RESEARCH ARTICLE



Enhanced electrochemical performance of 3-D microporous nickel/nickel oxide nanoflakes for application in supercapacitors

Balwant Kr. Singh¹ | Debabrata Das¹ | Navid Attarzadeh^{1,2} | Srija N. Chintalapalle¹ | Chintalapalle V. Ramana^{1,3}

Correspondence

Chintalapalle V. Ramana, Centre for Advanced Materials Research (CMR), University of Texas at El Paso, 500 W University Ave, El Paso, Texas 79968, USA. Email: rvchintalapalle@utep.edu

Abstract

Increasing energy demands, depletion of fossil fuels, and environmental issues have impelled society to choose the pathways of renewable and clean energy, which motivated scientists and engineers to develop sustainable, renewable, and clean energy resources. However, the major challenge is the implementation of low-cost, flexible approaches and materials to fulfill the requirements of energy storage and conversion technologies, specifically those involving batteries and supercapacitors. In this context, herein, we demonstrate an integrated approach to realize three-dimensional (3-D) mesoporous nickel(Ni)/nickel oxide (NiO) nanostructures with enhanced performance for supercapacitor applications. Conformal deposition of NiO nanoflakes on 3-D mesoporous Ni onto inexpensive Cu substrates with large active surface area, providing easy ion accessibility through mesoporous channels and improving electron transport through interconnected nickel network. The 3-D mesoporous Ni/NiO nanoflakes exhibit excellent electrochemical performance, namely, areal capacitance of 720 mFcm⁻², energy density of 4 μ Whcm⁻² and power density of 2.5 mWcm⁻² and a reasonable capacity retention for 5000 cycles. We believe that these results may provide a roadmap to further tune the conditions so as to engineer oxide architectures to derive enhanced energy performance of supercapacitor devices for practical applications.

KEYWORDS

3-D mesoporous nickel, electrodeposition, nanoflakes, nickel oxide, supercapacitor

1 | INTRODUCTION

Global warming, greenhouse gas emissions, climate change, rising energy demand, and fossil fuel depletion have pushed society towards clean and sustainable energy technology. Clean energy generation from renewable sources like solar, wind and hydro are possible solutions, but they are intermittent in nature. [1-3] Therefore, energy storage and conversion technologies are necessary for continuous energy supply. The demand for energy storage

This is an open access article under the terms of the Creative Commons Attribution License, which permits use, distribution and reproduction in any medium, provided the original work is properly cited.

© 2023 The Authors. Nano Select published by Wiley-VCH GmbH.

Nano Select 2023;4:145–159. wileyonlinelibrary.com/journal/nano

¹Centre for Advanced Materials Research (CMR), University of Texas at El Paso, El Paso, Texas, USA

²Environmental Science and Engineering, University of Texas at El Paso, El Paso, Texas, USA

³Department of Mechanical Engineering University of Texas at El Paso, El Paso, Texas, USA

units are also increasing due to their application in electric vehicles and portable electronic devices. [4] Batteries and supercapacitors are most widely used for energy storage devices. The high energy density (~180 Whkg⁻¹) of batteries makes it first choice for consumer electronics devices, but its low power density, sluggish charge transport and dendrite formation at high power leads to failure. On the other hand, the high power density (~10 Wkg⁻¹), fast charge-discharge time, and longer cyclic life (>100,000) makes supercapacitor useful by complimenting batteries or replacing it in some applications. [5-7] To achieve high energy density, different transition metal oxides have been used but most of them suffer from poor electrical conductivity, except ruthenium oxide. The high cost of ruthenium oxide is an obstacle for its bulk application.

Nickel oxide (NiO), which is one among transition metal oxides, find widespread applications in different domains due to its structural, electronic, optical, and electrochemical properties.^[8-10] NiO finds application as a p-type photo-electrode in dye-sensitized solar cell,[11] ammonia sensors, [12] electrocatalyst for oxygen evolution reaction (OER),[13] cathode material for quasi-solid state lithium ion battery, [14] and electrochemical capacitor. [15] Previously, we demonstrated the possibility for giant dielectric permittivity ($\varepsilon \sim 10^4$ or higher) in NiO doped with lithium and/or titanium. [16] Additionally, the Ni-Fe oxide system exhibits interesting features for using those materials for electronic devices, such as traditional dielectric capacitors for semiconductor microelectronics. [17] Furthermore, NiO is also a promising candidate in electrochemical energy applications, primarily due to its reduced cost, greater abundance, nontoxicity, environmental stability, and acceptable electrochemical characteristics with good thermal stability. [8,18,19] The theoretical capacitance of NiO is 3750 Fg⁻¹, which is higher than other pseudocapacitive materials MnO₂ (1370 Fg⁻¹) and hydrated RuO₂.nH₂O (2200 Fg⁻¹) for supercapacitor applications. [19,20] However, as reported in the literature, NiO exhibits electrical conductivity $(10^{-13} \Omega \text{cm}^{-1})$ at room temperature typically categorized as a Mott-Hubbard insulator. [21,22] Also, the properties and applications of NiO are sensitive to the processing conditions and methods employed for synthesis. NiO materials were synthesized by different processing techniques, such as electron beam evaporation, [22] hydrothermal,^[24] chemical bath deposition,^[25] sol-gel process, [26] chemical precipitation, [27] microwave mediated synthesis, [18] and electrochemical deposition. [28] Compared to other processing methods, electrodeposition has multiple advantages, namely, the low cost and precise control on the resulting nanostructures' shape, size, thickness, and mass loading.[29-32]

In the present work, using simple, lost-cost processing by electrodeposition, we demonstrate enhanced perfor-

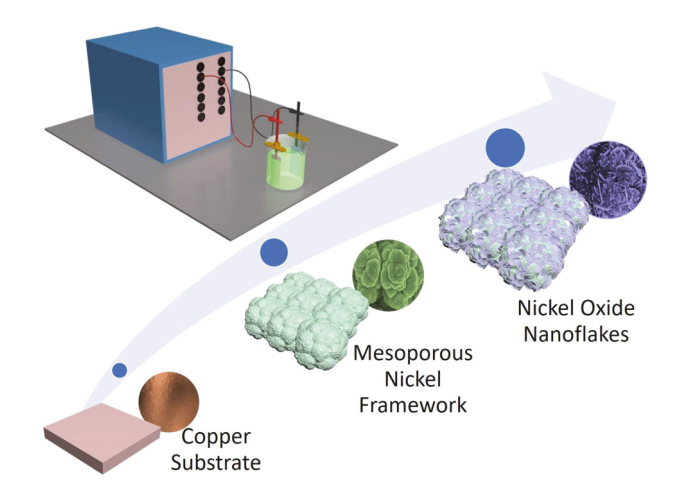


FIGURE 1 Schematic for electrodeposition process of 3-D mesoporous Ni/NiO nanoflakes

mance of 3-D mesoporous Ni/NiO nanoflakes as active electrode materials for supercapacitor with a high-rate capability. Note that the surface area and electrical conductivity are the most important factors affecting the performance of a supercapacitor.[33,34] Three-dimensional (3-D) porous interconnected metal network provides extremely higher surface-to-volume ratio in addition to the ease of the ion-diffusion path. Therefore, conformal deposition of metal oxide on 3-D porous metal not only improves electrical conductivity but also provide binder-free electrode materials.[35] In fact, nanoporous gold (Au) with interconnected porous network is widely used for energy storage and conversion devices, such as batteries, [36] supercapacitors, [37] and electrocatalysis. [38] However, the high cost of gold hindered its use for commercial and bulk of the applications. Therefore, it is highly important to research low-cost alternatives for making porous metal. Nickel fulfills low-cost option with almost similar properties and is used in the form of films, foils, and foam for all energy related applications. However, in most of the cases, Ni substrate procured in different forms and used for deposition of active materials by different processes, which again increase the fabrication cost etc. [24,39,40]

Herein, we demonstrate economically viable method of making Ni/NiO 3-D mesoporous nanoflakes as active electrode materials onto an inexpensive Cu substrates and illustratively present their enhanced performance in a supercapacitor that too with a high rate capability. The approach (Figure 1) rely on conformal electrodeposition of NiO nanoflakes on 3-D mesoporous Ni skeleton to reduce interface contact resistance by providing ease of ion accessibility through mesoporous channels and improved electron transport through interconnected porous Ni network. As presented and discussed in this contribution, the 3-D mesoporous Ni/NiO nanoflakes exhibit excellent electrochemical performance, where the supercapacitor device

performance is characterized by an areal capacitance of 720 mFcm $^{-2}$, energy density of 4 μ Whcm $^{-2}$, power density of 2.5 mWcm $^{-2}$, with a reasonable capacity retention (80%) after 5000 cycles. We believe that the approach demonstrated can be applicable to a large of class of mesoporous 3-D network design of the metal/metaloxide framework for application or efficient design of the integrated electrochemical devices.

2 | RESULTS AND DISCUSSION

2.1 | Structure, morphology, and elemental composition

2.1.1 | Crystal structure and phase

X-ray diffraction (XRD) analyses were employed to understand the phase composition of the deposited materials. Figure 2 shows the XRD pattern of microporous Ni deposited at different current density and NiO nanoflakes grown on microporous Ni (NPN-100) as a function of time. All the samples in Figure 2 show the peaks at 44.33°, 44.47°, 51.4°, 51.81°, 74.9°, and 77.33°. The peaks at 44.33, 51.4, and 74.9° correspond to the diffraction from (111), (200), and (220) planes of metallic Cu, as matched with ICDD number 00-003-1018. The peaks at 44.47, 51.81, and 77.33° corresponds to the diffraction from (111), (200), and (220) planes of metallic Ni, as matched with ICDD 00-03-1015. Cu and Ni peaks are in good agreement with existing literature. [41] The absence of NiO peak may be due to its amorphous nature.

2.1.2 | Surface morphology

The scanning electron microscopy (SEM) imaging analyses employed to understand the surface morphology and feature size of Ni/NiO materials developed for supercapacitor applications. Figure 3 shows that morphology of the samples with increasing deposition current. The surface roughness and porosity increases, as evident in Figure 3, with increasing current. At low current density (25 mAcm⁻²), as shown in Figure 3A, the surface looks compact without any appreciable space between the particles, with increasing current density from 50 mAcm⁻² to 150 mAcm⁻², the surface roughness and particle size increases, as seen in Figure 3B–F. The three-dimensional (3-D) microporous Ni network looks like cauliflower fioretto (see, Figure 3D–F).

The NiO nanoflakes were grown on microporous Ni (NPN-100), which provide a porous template, by maintaining a constant current of 1 mAcm⁻² for the fabrication

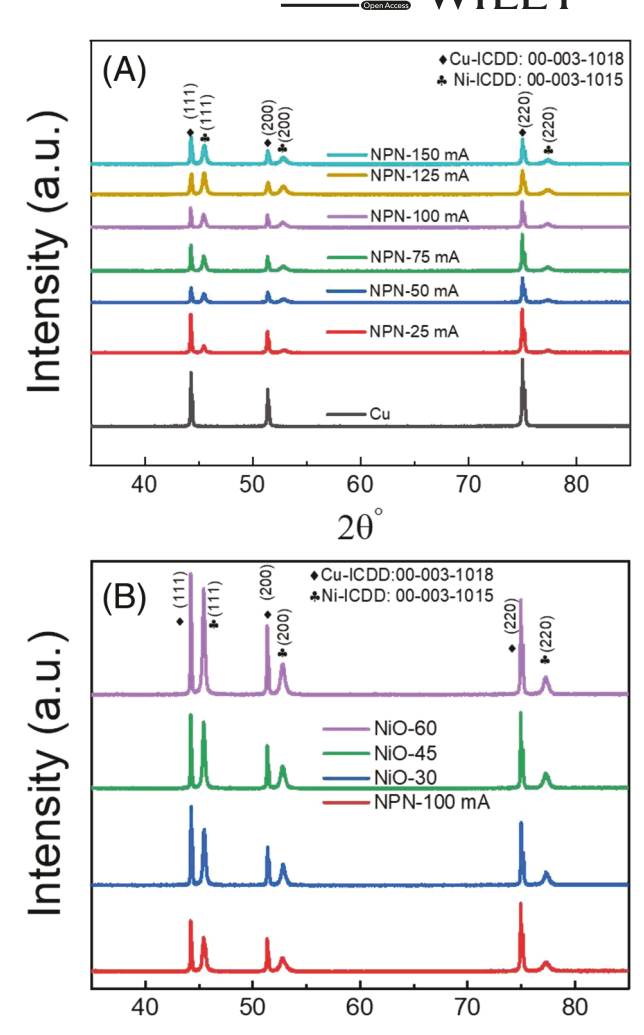


FIGURE 2 X-ray diffraction pattern of (A) microporous nickel on copper substrate deposited at different current density (25–150 mAcm⁻²) for 180 s deposition time and (B) nickel oxide nanoflakes deposited on microporous nickel at 1 mA cm⁻² for the duration 30, 45, and 60 min

 $2\theta^{\circ}$

time varying from 0 to 1 h (60 min). The SEM data of NiO nanoflakes grown on the Ni template are shown in Figure 4. It can be seen that the sharpness of microporous Ni edge fades off with the deposition of NiO nanoflakes (Figure 4A–C). The size of NiO nanoflakes also increases with increase in deposition time, as evident in SEM images shown in Figure 4D–F. NiO nanostructures constructed into a well-defined morphology, which seems like nanoflakes, on three-dimensional microporous Ni after 60 min of deposition (Figure 4F).

The specific variation in the feature size of NiO nanoflakes has been calculated using the SEM analyses. Specifically, the diameter of the particles was determined from SEM images by using image J software. [42] The statistical data and mean diameter obtained are shown in Figure 5. It is evident that, with increasing the deposition

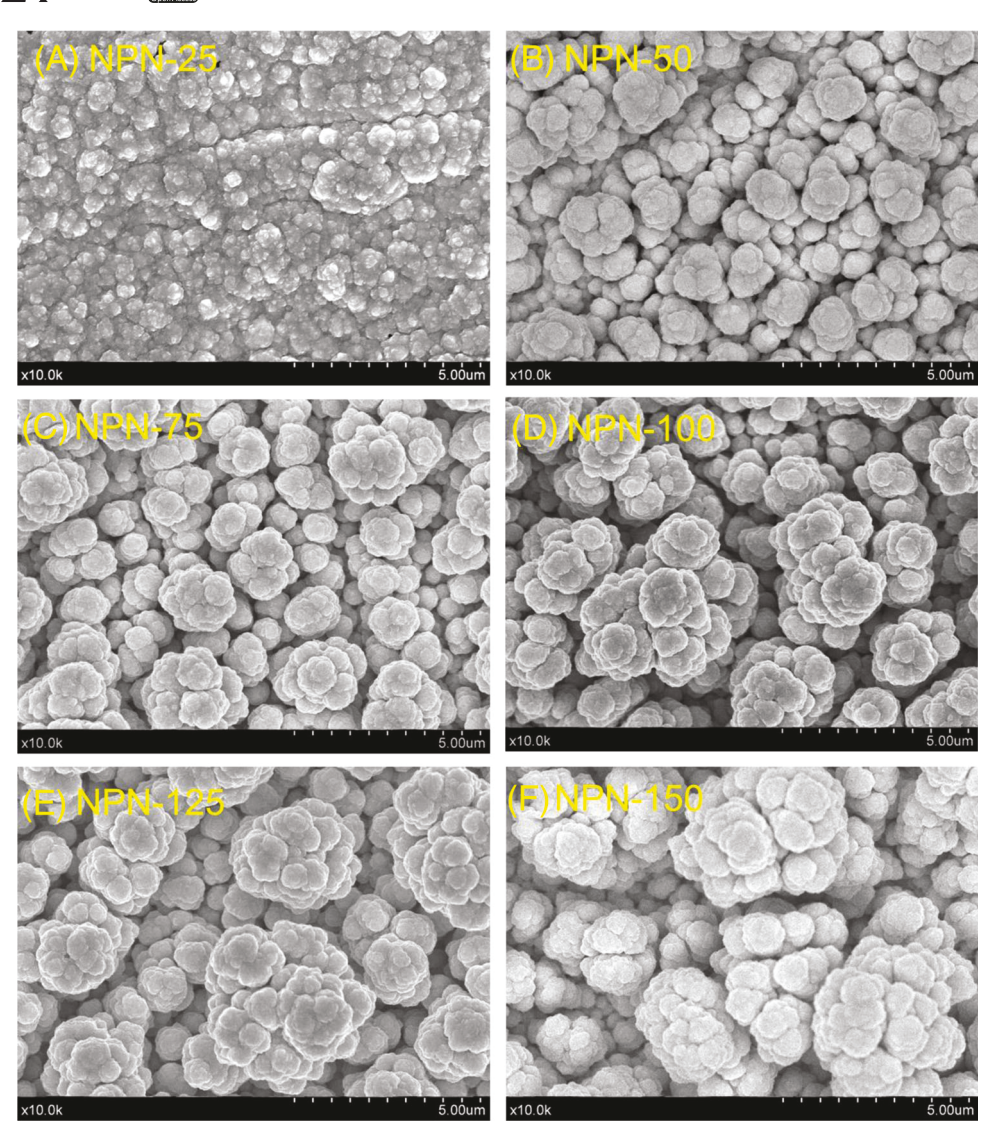


FIGURE 3 SEM images of microporous nickel deposited on copper substrate at different current density for duration of 180 sweek: (A) 25 mAcm⁻², (B) 50 mAcm⁻², (C) 75 mAcm⁻², (D) 100 mAcm⁻², (E) 125 mAcm⁻², and (F) 150 mAcm⁻²

time, the mean diameter of NiO nanoflakes found to be increasing. The mean diameter of NiO nanoflakes is 74, 84, and 110 nm, respectively, for the deposition time of 30, 45, and 60 min, as shown in Figure 5.

2.1.3 | Elemental composition and homogeneity

Energy dispersive X-ray spectroscopy (EDS), where the characteristic X-ray energy is the signature of the atom present in the sample, [43] analyses allowed us to identify the elemental composition as well as elemental distribution profiles in Ni/NiO materials. Figure S1 shows the images and corresponding EDS spectra for NiO nanoflakes deposited under variable processing time. Spectral images clearly depict that the concentration of NiO increases with

increasing deposition time. With increasing time, atomic percentage (at%) of Ni decreasing while oxygen at% is increased, and it indicates that the highest amount of NiO nanoflakes present for samples with a fabrication time of 60 min. This is what expected and desirable to obtain a 3-D-conformal coverage of NiO nanoflakes on top of mesoporous Ni. Figure S2 shows the elemental mapping images of NiO nanoflakes deposited on microporous Ni under variable deposition time. It is evident that the samples are chemically homogeneous and elemental distribution evenly on the samples' surfaces.

2.2 | Spectrophotometric analysis

As microporous Ni on copper substrate is opaque in UV-vis-NIR region, the NiO nanoflakes at top probed in

FIGURE 4 SEM images of electrodeposited nickel oxide nanoflakes on 3-D microporous nickel skeleton at current of 1mAcm⁻² for different durations, for low magnification (x10k): (A) 30 min (C) 45 min and (E) 60 min, for high magnification (x70k): (B) 30 min (D) 45 min, and (F) 60 min

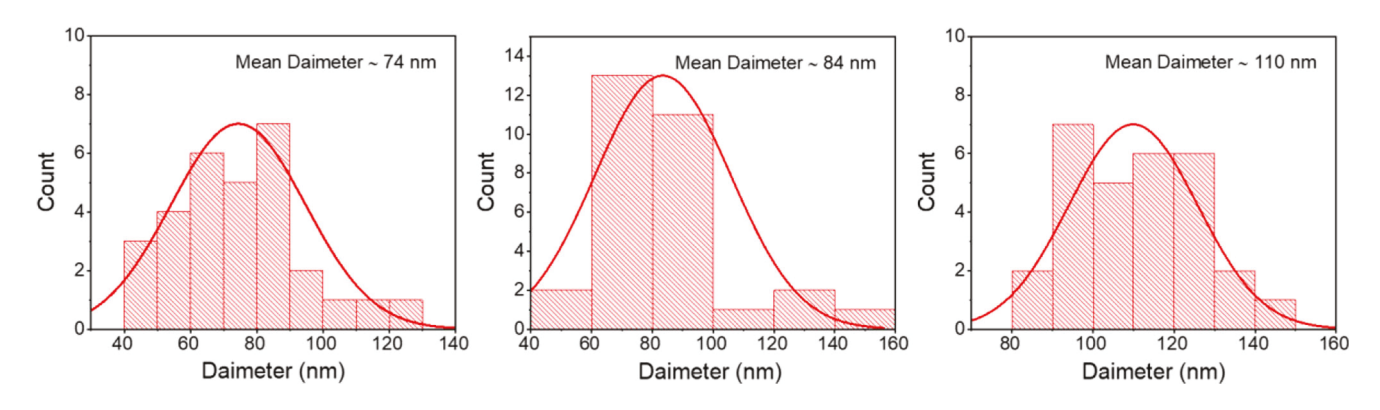


FIGURE 5 The variation of feature size of NiO nanoflakes with deposition time. The mean diameters estimated for the deposition time of (A) 30 min, (B) 45 min, and (C) 60 min are shown

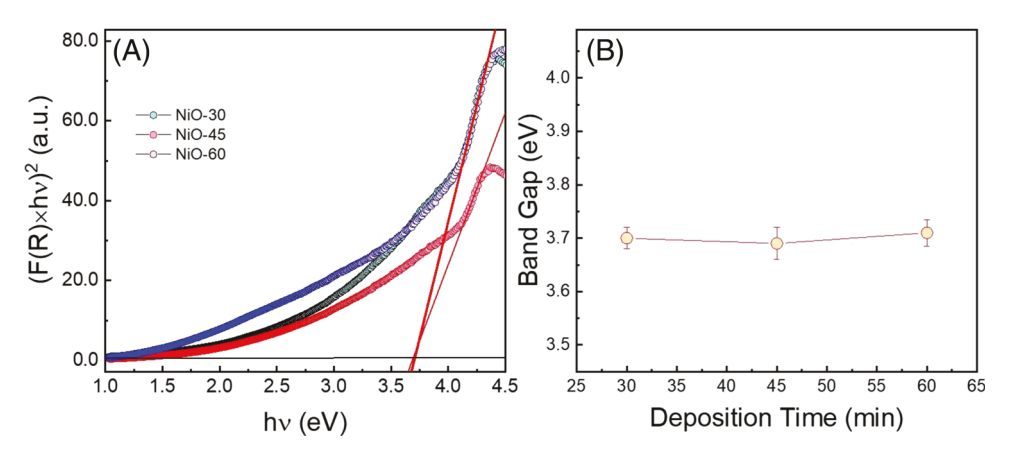


FIGURE 6 A, Tauc plot for the determination of bandgap, linear part of the plot is extrapolated to the x-axis. B, Bandgap of NiO nanoflakes as a function of deposition time

diffused reflectance mode. The expectation is that the spectrophotometric measurements distinguish the formation of NiO nanoflakes, which are distinct from microporous Ni metal in terms of optical and electronic properties, especially such measurements may allow the assessment of semiconductor properties of NiO nanoflakes as desirable for electrochemical energy or capacitor applications. The Kubelka-Munk (KM) formalism^[44–47] was applied to calculate the band gap from diffused reflectance spectrum; the KM function is defined as:

$$F(R) = \frac{K}{S} = \frac{(1-R)^2}{2R} \tag{1}$$

Here, F(R), K, S, and R represent the KM function, absorption coefficient, scattering coefficient, and reflectance, respectively. KM function replicates the behavior of absorption coefficient and can be used to calculate optical band-edge transition of the NiO nanoflakes, as presented here. The Tauc Equation (2) has been modified accordingly and executed to calculate the band gap of nanotextured NiO layers as a function of deposition time.

$$F(R) \times hv = A(hv - E_g)^n \tag{2}$$

Here, h, v, E_g , F(R) and A represents the Planck constant, incident photon frequency, optical band gap, KM function, and fitting parameter, respectively. n=0.5 represents direct optical transitions. The data shown in Figure 6 fits very well to Equation (2) confirming the direct band gap semiconductor nature of the NiO nanoflakes deposited.

All the NiO nanoflakes samples indicate the direct optical band gap located at 3.7 eV, which is very similar to bulk or thin film NiO on various platforms. Thus, these special measurements complement our XRD and SEM-EDS data, shown earlier. The reflectance data, shown in Figure S3, along with Tauc plots in Figure 6A show a

gradual transition, starting from NIR region. This particular behavior is well-known for oxygen deficient NiO. We have deliberately optimized these samples in such a way to incorporate energy states owing to oxygen vacancies and improve the overall conductivity of as grown nanostructed NiO nanoflakes. Almost similar direct optical transition in all the samples (Figure 6B) confirms the structural and compositional integrity throughout the process. Thus, our processing efforts successfully results in the NiO nanoflakes with only the porosity in nanometer range tailored to enhance the electrochemical performance. After thorough and deeper studies establishing the formation of well-defined NiO nanoflakes with desirable structure and morphology features, we performed detailed electrochemical studies to evaluate their performance in supercapacitors and also validate the hypothesis that the 3-D interconnected network provides enhanced energy performance.

2.3 | Electrochemical characterization

2.3.1 | Cyclic voltammetry

The electrochemical characterization of all the NiO samples was carried out in a three-electrode system, where platinum and Ag/AgCl were used as counter and reference electrodes. Figure 7 shows the cyclic voltammetry (CV) plots of microporous Ni prepared at variable deposition current in 1 M Na₂SO₄ at 50 mVs⁻¹. Figure 7A shows the almost rectangular electricaldouble-layerr current versus potential plot. The area under the curve is increasing from NPN-25 to NPN-100, but the current in NPN-125 and NPN-150 is less than in NPN-100. So, NPN-100 has higher area under the curve. The capacitance versus deposition current data are plotted in Figure 6B. The capacitance value is also increasing with deposition

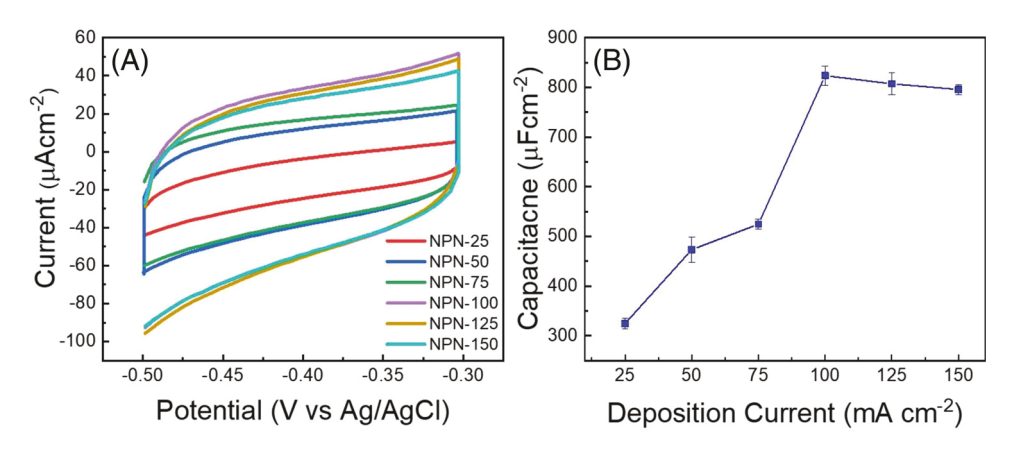


FIGURE 7 A, Cyclic voltammetry (CV) of microporous nickel samples at 50 mVs $^{-1}$ scan rate in 1 M Na₂SO₄ and (B) variation of capacitance with change in deposition current, calculated from CV at 50 mVs $^{-1}$

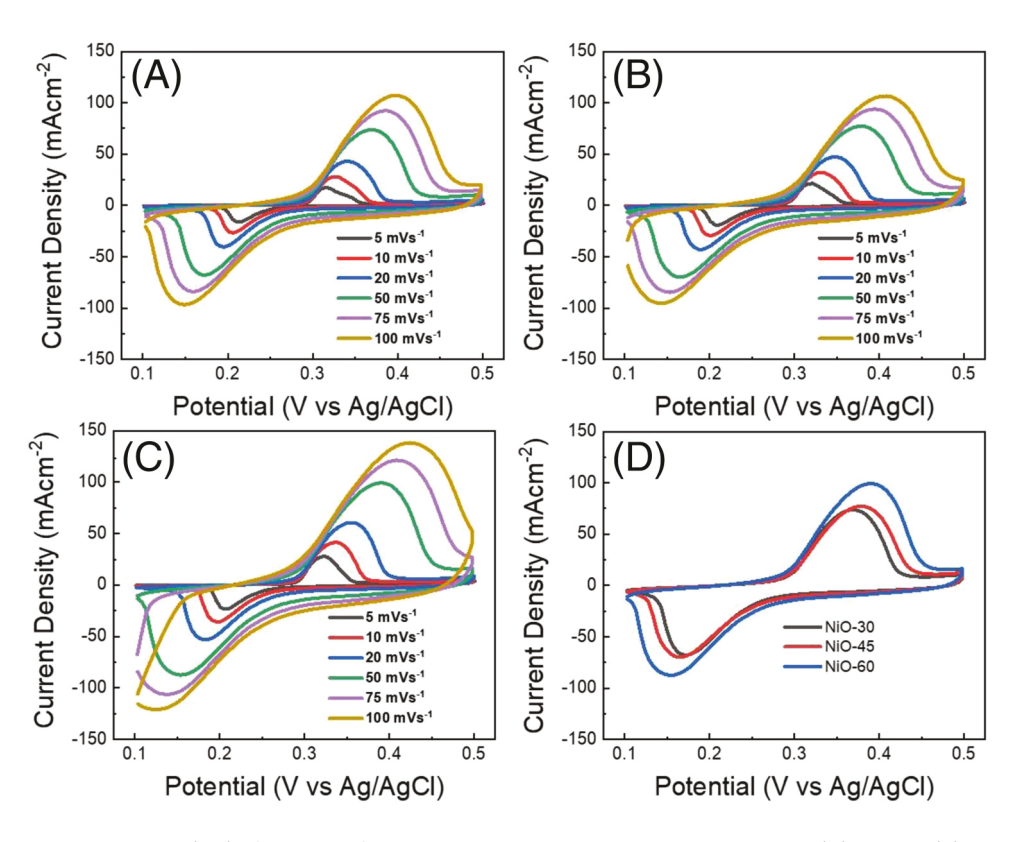


FIGURE 8 Cyclic voltammetry (CV) of NiO nanoflakes deposited under variable deposition time. (A) 30 min, (B) 45 min, (C) 60 min, and (D) comparison of voltammograms at 50 mVs⁻¹

current. It has the maximum value of $823 \pm 20 \,\mu\text{Fcm}^{-2}$ at $100 \, \text{mAcm}^{-2}$ deposition current and, then, it decreases. The double layer capacitance is directly proportional to surface area of materials. Therefore, it is confirmed that the microporous Ni deposited at $100 \, \text{mA cm}^{-2}$ has higher surface area than others. Hence, porous Ni deposited at $100 \, \text{mAcm}^{-2}$ was used for the growth of NiO nanoflakes.

The CV and galvanic charge-discharge (GCD) of all NiO nanoflakes samples were performed in 3 M KOH in three

electrode system. The CV curves of NiO samples were recorded at different scan rates 5 mVs⁻¹- 100 mVs⁻¹, as shown in Figure 8A–C. In all the samples, the current increases with increasing scan rate indicating capacitive nature of NiO nanoflakes. The pair of anodic and cathodic peaks between 0.1 V to 0.4 V shows the faradaic redox mechanism of Ni²⁺ to Ni³⁺, indicating pseudocapacitive nature of NiO nanoflakes similar to that previously reported in literature.^[24,49] The pair of redox reactions

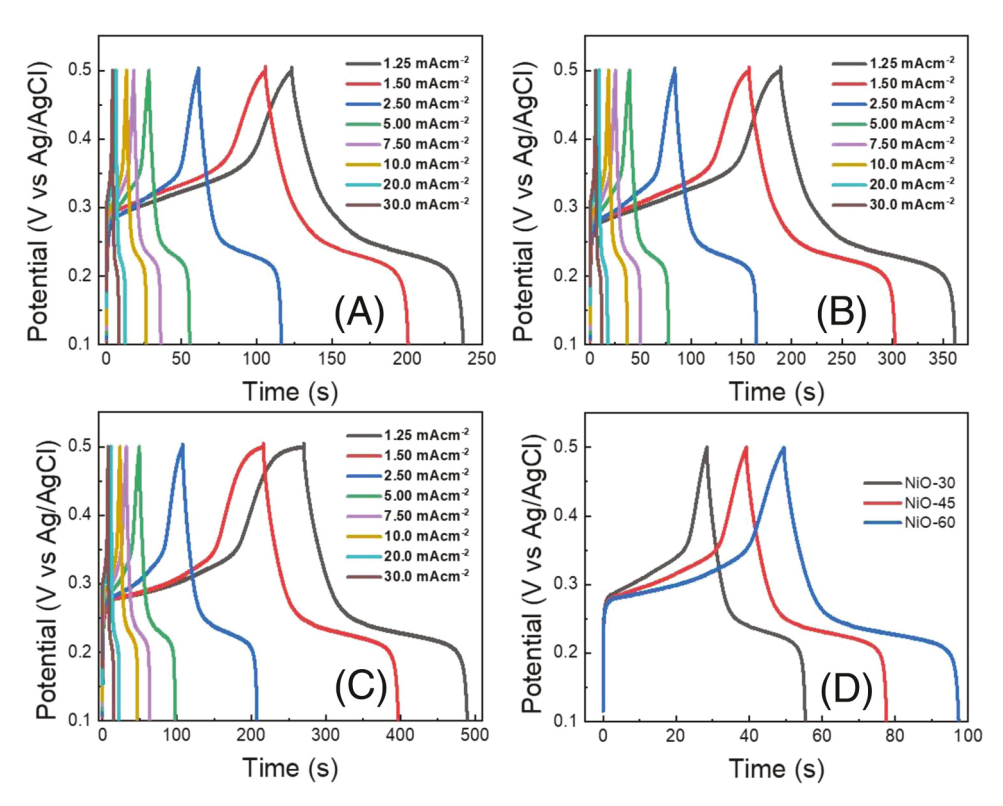


FIGURE 9 Galvanic charge-discharge (GCD) profiles of NiO nanoflakes fabricated at variable deposition time. The data shown are for samples deposited at: (A) 30 min, (B) 45 min, (C) 60 min, and (D) comparison of charge-discharge curves at 5mAcm⁻².

during oxidation and reduction can be explain by following equation [19,50]:

$$NiO + OH^- \leftrightarrow NiOOH + e^-$$
 (3)

The comparisons of CV curves of NiO nanoflakes prepared under different deposition times at 50 mVs⁻¹ are shown in Figure 8D. Here, the current increases with increasing deposition time and NiONiO samples deposited at 60 min exhibit maximum area under the curve.

2.3.2 | Galvanic charge-discharge profiles

The galvanic charge discharge (GCD) curves of the NiO nanoflakes were obtained at different current density, which is varied from 1.25 mAcm⁻² to 30 mAcm⁻² in a potential window of 0.1 to 0.5 V similar to CV potential window. Figure 9 shows the charge-discharge curves of NiO nanoflakes. The data shown (Figure 9A–C) are for NiO samples deposited at 30, 45, and 60 min, respectively. In all the samples, charging and discharging time are increasing with decreasing current density. In all the cases, the higher discharge time was obtained at current density of 1.25 mAcm⁻². The nonlinear nature of GCD shows pseudocapacitive nature of NiO nanoflakes similar to the

CV curves.^[18] Figure 9D shows the comparison of all NiO samples at a current density of 5 mAcm⁻². Nickel oxide deposited at 60 min shows higher discharge time, signifying better storage performance of NiO samples deposited at 30 and 45 min.

The variation of specific capacitance with different scan rate for NiO samples is shown in Figure 10A. In all the samples, the specific capacitance increases with decreasing scan rate. This is due to the fact that, at lower scan rates, the electrolyte ions have longer time to get to the bulk of NiO nanoflakes, while, at higher scan rates, ion movement is limited to the near surface.^[37] The highest specific capacitance of 720, 557, and 435 mFcm⁻² was achieved at 5 mVs⁻¹ for NiO samples deposited at 30n, 45, and 60 min, respectively. The charge storage process of an electrode material can be calculated from CV by plotting the peak current as a function of scan rate. If the peak current is directly proportional to scan rate, it is called surface charge storage process. On the other hand, if peak current is proportional to square root of scan rate, it is classified as a semi-infinite bulk diffusion process. These can be expressed, respectively, by the following equations^[51,52]:

$$i = av^b \tag{4}$$

$$logi = loga + blogv (5)$$

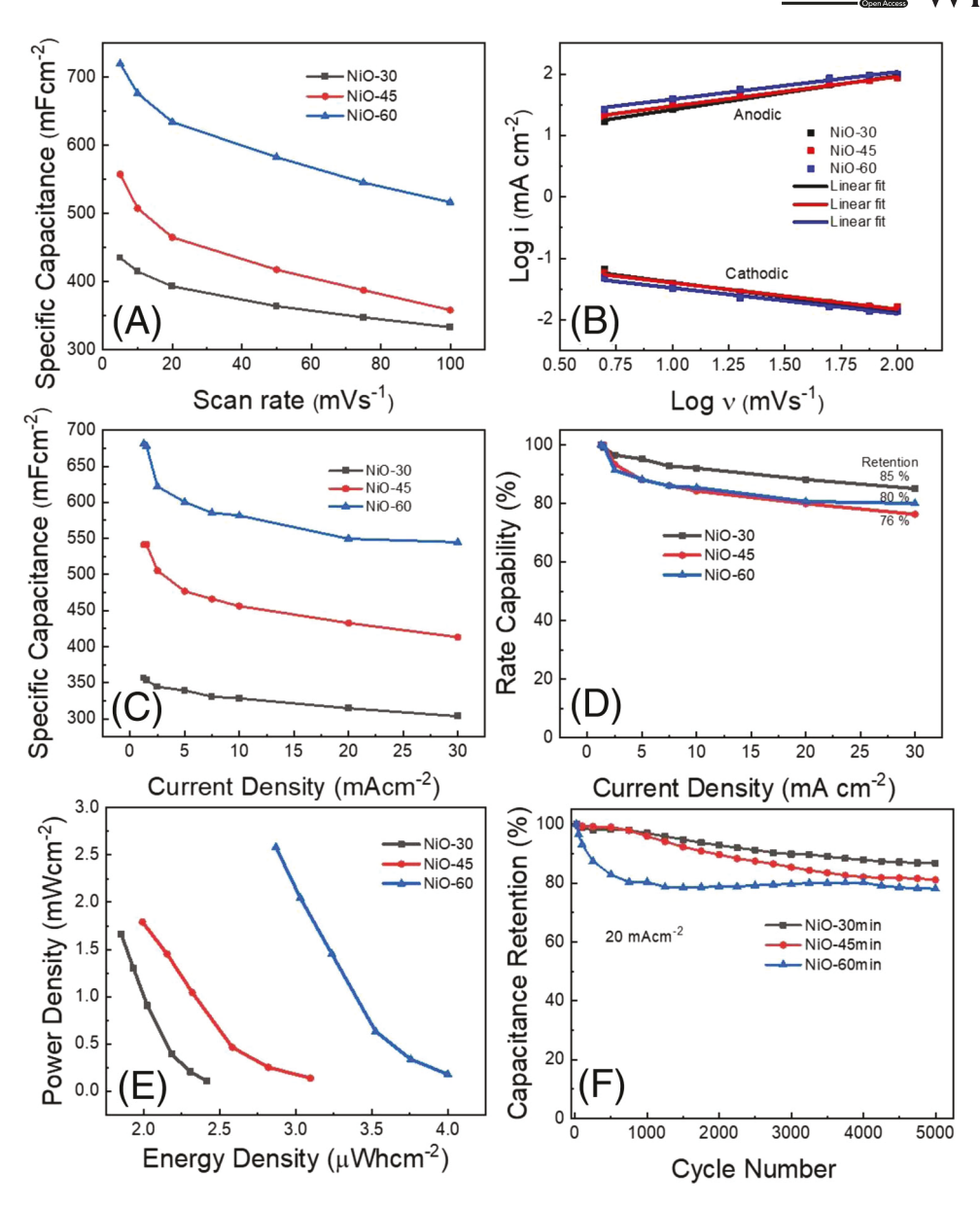


FIGURE 10 A, Specific capacitance at different scan rates, (B) peak current versus scan rate, (C) variation of specific capacitance with current density and (D) rate capability variation with respect to current density, (E) Ragone plot of nickel oxide nanoflakes at different scan rate (F) cyclic stability test of Ni/NiO nanoflakes at current density of 20 mAcm⁻².

where i is the peak current and a and b are the adjustable constants. The constant b takes b=1 and b=0.5 for capacitive and diffusion controlled processes, respectively. Figure 10B shows the linear relation between log of peak current versus log of scan rate for all the NiO nanoflake samples. The value of b calculated from fitting procedure are 0.55, 0.48, 0.45 and 0.48, 0.44, 0.42 for anodic and cathodic peaks for 30, 45, and 60 min deposited NiOs, respectively. Within the range, the value of is equal to nearly 0.5 in all the cases, and it indicates that the diffusion controlled mechanism is operative in NiO nanoflakes. Figure 10C shows the variation of specific capacitance with respect to current density. It is evident

that the specific capacitance decreases with increasing current density in all the NiO samples. The maximum specific capacitance is obtained in NiO nanoflakes deposited for 60 min. The highest specific capacitance of 681, 541, and 356 mFcm⁻² was achieved at current density of 1.25 mAcm⁻² for deposition time of 30, 45, and 60 min, respectively. For high-performance supercapacitor devices, the ability to maintain high capacitance during rapid charging/discharging is crucial and it is defined by term called rate capability or rate performance.^[53,54] The rate capability of NiO nanoflakes at a current density of 1.25 mA cm⁻² to 30 mA cm⁻² is presented in in Figure 10D. The rate capability of NiO-30, NiO-45, and NiO-60 is 85,



TABLE 1 Comparison of performance of NiO nanoflakes (present work) with different metal oxides in a three-electrode system

Electrodematerial	Specific capacitance	Scan rate/ current density	Electrolyte	Rate performance	Cyclic stability	Ref.
Ni/NiO core/shell	566 mFcm ⁻²	$2~\mathrm{mVs^{-1}}$	1 M KOH	39% from 2 to 100 $\mathrm{mVs^{-1}}$	57% after 1200	[49]
CuO/Cu ₂ O@CoO nanowire arrays	280 mFcm ⁻²	1 mAcm ⁻²	2 M KOH	53% from 5 to 100 mVs ⁻¹	90.7% after 3000	[54]
NiO nanoflake	74.8 mFcm ⁻²	$10~\mathrm{mVs^{-1}}$	1 M KOH	66% from 10 to 100 mVs^{-1}	100 % after 5000	[56]
NiO film	$68\mu\mathrm{Fcm^{-2}}$	$5~\mathrm{mVs^{-1}}$	3% KOH	-	-	[57]
Co(OH) ₂ nanosheet	22.93 mFcm^{-2}	$5~\mathrm{mVs^{-1}}$	2 M KOH	61% from 5 to 200 $\rm mVs^{-1}$	90 % after 10000	[58]
Copper oxide nanowires	320 mFcm^{-2}	$5~\mathrm{mVs^{-1}}$	3 М КОН	$39 \% \text{ from 5 to } 200 \text{ mVs}^{-1}$	115 % after 5000	[59]
2D- LiCoO ₂	310 mFcm ⁻²	$5~\mathrm{mVs^{-1}}$	1 M LiCl	$38~\%$ from 5 to 100 mVs^{-1}	80.3 % after 2000	[60]
MnO_2/MoS_2	224 mFcm ⁻²	$0.1~\mathrm{mAcm^{-2}}$	$1\mathrm{M}\mathrm{Na_2SO_4}$	70.5% from 0.1 to 1 mFcm ⁻²	90 % after 3000	[61]
NiO thin film	23.4 mFcm^{-2}	$5~\mathrm{mVs^{-1}}$	1 M LiClO ₄ -PC	${\sim}50~\%$ from 5 to 200 mVs^{-1}	_	[62]
NiO nanoflakes	870 mFcm ⁻²	$1\mathrm{mAcm^{-2}}$	3 М КОН	-	84 % after 6000	[63]
3-D Ni/NiO nanoflakes	720 mFcm ⁻²	$5~\mathrm{mVs^{-1}}$	3 М КОН	76 % from 1.25 to 30 mFcm ⁻²	78 % after 5000	This wor

76, and 80% respectively, which is much better compared to other metal oxides. For comparison and to understand the better rate capability of these NiO nanoflakes, the obtained data are compared with the literature in Table 1.

Ragone plot shows the relationship between energy density and power density of NiO at different scan rates. NiO nanoflakes show maximum energy density of 4 μ Whcm⁻² at 5 mVs⁻¹, power density of 2.5 mW cm⁻² at 100 mVs⁻¹ in the case of NPN-60, as shown in Figure 10E. The cyclic stability tests performed at current density of 20 mAcm-2 for all NiO nanoflakes and the data are shown in Figure 10F. It is evident that the NiO nanoflakes show excellent cyclic stability of 87, 81, and 78% after 5000 cycles for deposition time of 30, 45, and 60 min, respectively.

2.3.3 | Stability after cycling

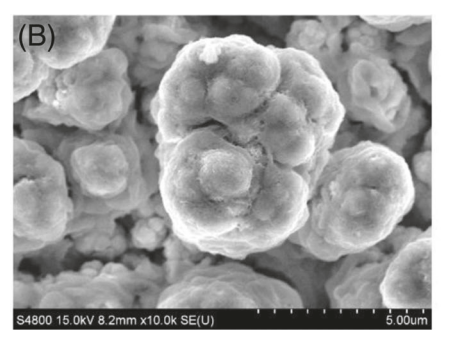
In order to understand the material stability or degradation (if, any) after cycling, we performed the SEM, EDX, and optical absorption studies. The measurements were carried out on the NiO samples after 5000 cycles. The SEM data of the samples after cycling are presented in Figure 11. It is evident that, after cyclic stability, NiO nanoflakes still exhibit the 3-D Ni skeleton morphology after 5000 cycles. It is remarkable that, although the overall capacity fades off to 80%, the morphology and 3-D interconnected network is quite stable even after 5000 cycles. The attempts made to understand the elemental composition also indicate that the original composition retained very well. Figure 12 shows the EDX of NiO samples after 5000 cycles. The EDX spectra show that the atomic percentage of oxygen increases slightly after cycling. Since there is a slight varia-

tion in terms of oxygen, we expect that there may be slight variation in the electronic behavior of the NiO nanoflakes. We relied on optical studies to confirm.

The optical spectra of the NiO nanoflakes samples after cycling are shown in Figure 13. The diffuse reflectance data of NiO samples after cycling for 5000 cycles are recorded under the same conditions as of the pristine samples. The obtained data are presented in Figure S4. As evident in Figure S4, no drastic changes are seen in the reflectance data, which is further used to calculate the K-M function and absorption, indicating that the electronic behavior of these NiO samples is also well maintained after cycling. While the overall optical behavior is very similar to the NiO before cycling, we observe a slight variation in the direct optical band gap. The data shown for representative samples in Figure 13 coupled with reflectance data in Figure S4 indicate that the NiO materials after cycling also exhibit a semiconductor band gap. The band gap reduction compared to intrinsic NiO nanoflakes before cycling may be due to the slight variations observed in EDX data. Thus, the SEM, EDX and electronic property measurements clearly indicate the material stability in terms of phase, composition, and material property after cycling. Overall, the stability studies after cycling are quite encouraging as the NiO nanoflakes still maintain the nanoscale porosity, which is the key to enhance their electrochemical performance in supercapacitors.

3 | CONCLUSIONS

We have successfully developed a cost-effective, facile process for the growth of three-dimensional (3-D) mesoporous



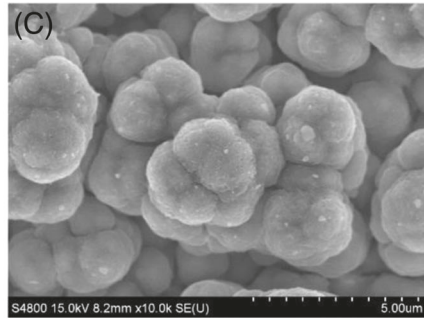


FIGURE 11 SEM images of nickel oxides nanoflakes samples after cyclic stability of 5000 cycles (A) 30 min, (B) 45 min, and (C) 60 min

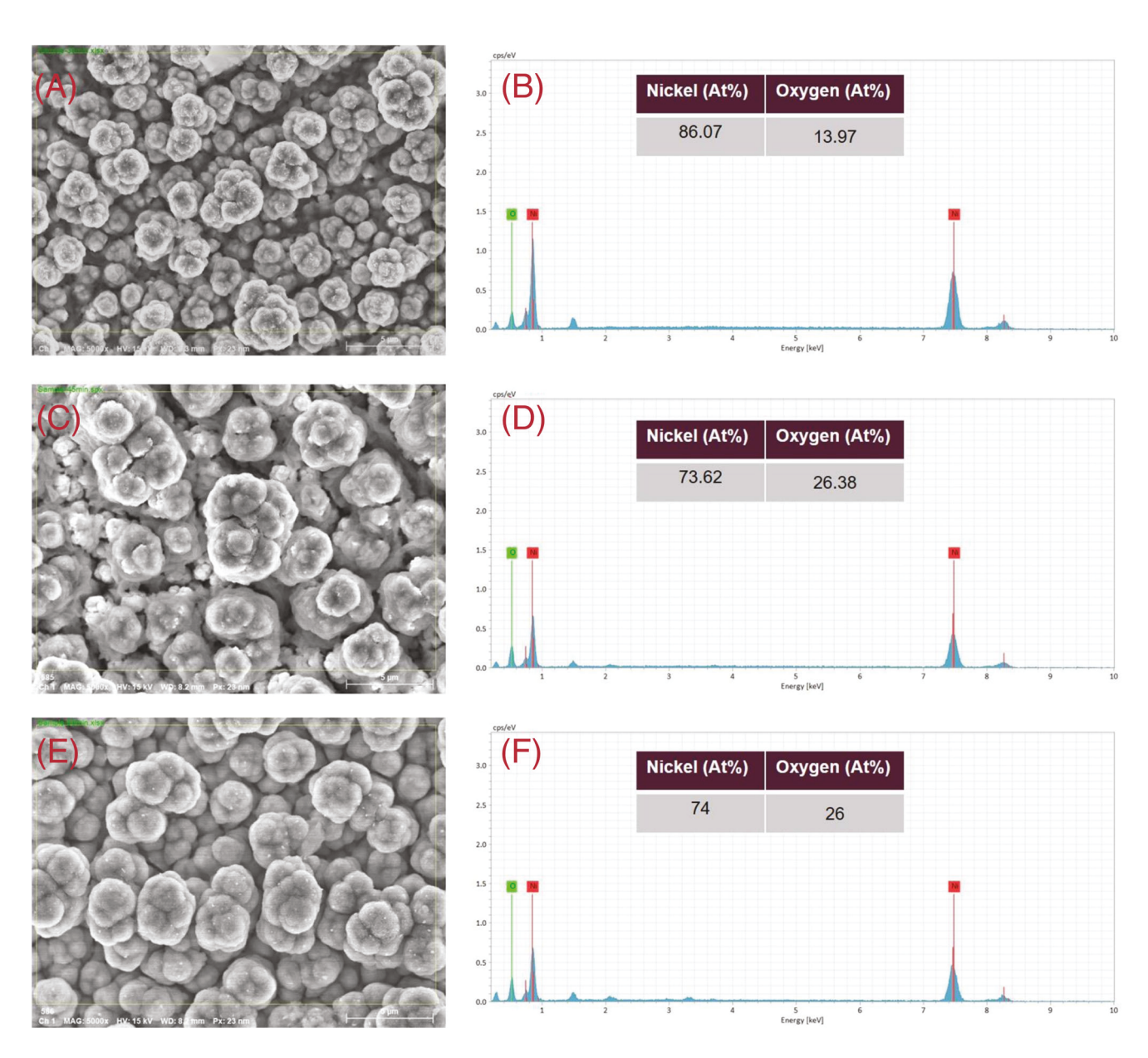
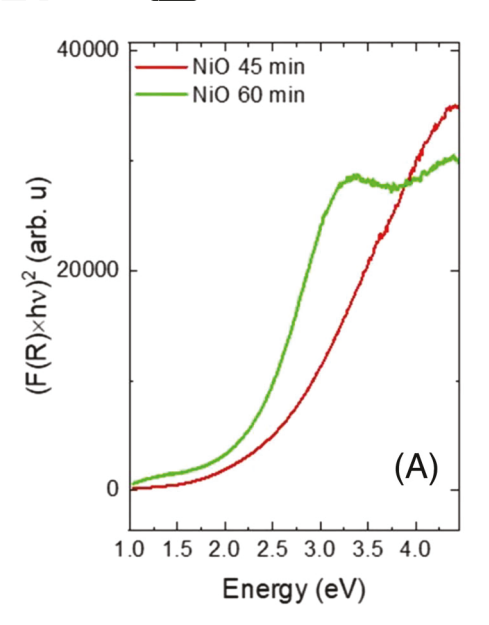


FIGURE 12 EDX images of nickel oxides nanoflakes samples after cyclic stability of 5000 cycles (A,B) 30 min, (C,D) 45 min, and (E,F) 60 min



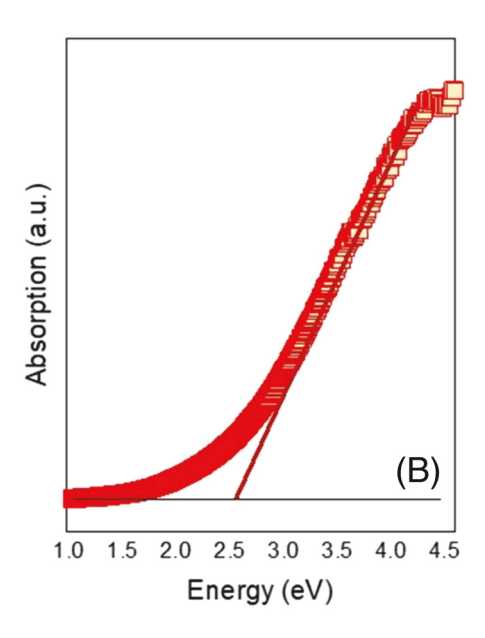


FIGURE 13 Tauc plots of the NiO samples after cycling. The plots indicate the K-M function for the determination of bandgap, where the linear part of the plot is extrapolated to the x-axis to obtain the band gap. The data clearly indicate that there is no deterioration of the material quality or properties of the NiO nanoflakes after cycling.

Ni and NiO nanoflakes for supercapacitors with demonstrated performance and high-rate capability. The optimization of the processing parameters in electrodeposition results in the deposition of 3-D mesoporous Ni/NiO onto economically feasible Cu substrates without need for much further preparation. The conformal deposition of NiO nanoflakes on 3-D mesoporous Ni with a large active surface area facilitates better ion accessibility across the mesoporous channels and increases electron transport through the linked Ni-network. As synthesized under the optimal conditions, the 3-D mesoporous Ni coupled with NiO nanoflakes exhibit enhanced electrochemical performance, with areal capacitance of 720 mFcm⁻², an energy density of 4 Whcm⁻², a power density of 2.5 mWcm⁻², and capacitance retention of 80% after 5000 cycles. The electron microscopy, elemental composition, and electronic property measurements demonstrate that the NiO nanoflakes exhibit excellent stability in terms of phase, composition, and material property after cycling to 5000 cycles. Under the proposed concept of Ni/NiO nanoflakes on inexpensive Cu substrates, the stability studies after cycling are quite encouraging as these NiO nanoflakes still maintain the nanoscale porosity, which is the key to enhance their electrochemical performance in supercapacitors. These results are expected to contribute significantly to the advancements in the field, and may provide a roadmap to further tune the conditions so as to engineer the selective architectures to derive further enhanced energy performance of supercapacitor devices for practical applications.

4 | EXPERIMENTAL SECTION

4.1 | Chemicals and reagents

All chemical reagents were of reagent grade and has been used without any further purification. Potassium hydroxide (KOH), hydrochloric acid (37%), nickel sulphate hexahydrate (NiSO₄.6H₂O), ammonium chloride (NH₄Cl), polyethylene glycol, sodium acetate, sodium sulphate (Na2SO₄) copper (99.98%), and sodium sulphate were purchased from Sigma–Aldrich. Distilled water has been used in all experiments for making solutions and cleaning.

4.2 | Electrodeposition of microporous Ni

The growth of microporous nickel on copper substrate was carried out using Galvanostatic electrodeposition process. The electrodeposition was performed using two electrode setup, where nickel foam and copper substrate were used as counter and working electrode, respectively. Prior to the deposition, copper substrate was cleaned in 1 M HCl solution and deionized water. The bath for the synthesis of microporous nickel was prepared by adding 0.12 M nickel sulphate hexahydrate, 1 M ammonium chloride, and polyethylene glycol (100 mg in 300 ml) in deionized water. [64] Then, the beaker containing aqueous bath was sonicated for 5 min to get stable light green solution. The electrodeposition was done at different

Dano WII FV 157

current 25, 50, 75, 100, 125 and 150 mAcm⁻² for 180 s. After the deposition, all samples were cleaned in deionized water and kept at 60°C for 1 h in an oven. The name of samples have allotted NPN-25, NPN-50, NPN-75, NPN-100, NPN-125, and NPN-150 corresponding to their deposition current.

4.3 | Electrodeposition of NiO nanoflakes

The nickel oxide nanoflakes were grown by the Galvanostatic electrodeposition process. The aqueous bath was prepared by adding 0.13 M sodium acetate, 0.13 M nickel sulphate and 0.1 M sodium sulphate. [61] The pH of the bath was maintained near 7 by adding 4–5 drop of KOH solution. The electrodeposition of nickel oxide nanoflakes was performed on microporous nickel (NPN-100 mAcm⁻²) at constant current density for 30, 45 and 60 min. After the deposition, all samples were washed with deionized water and kept at 200°C for 2 h in an oven.

The name of samples allotted as NiO-30, NiO-45, and NiO-60 respective to their deposition time.

4.4 | Material characterization

X-ray diffraction (XRD) patterns of mesoporous nickel and nickel oxide nanoflakes were recorded using a Malvern Panalytical Empyrean Nano edition multipurpose X-ray diffractometer. The X-ray diffractometer was used in Bragg-Brentano reflection geometry. All the measurements were performed at room temperature. A Cu Ka X-ray source with a wavelength of 0.154 nm was used to acquire the measurements. A Scanning Electron Microscope (SEM) was used to visualize the surface morphology of microporous nickel and nickel oxide nanoflakes. A Hitachi-4800 Field Emission Scanning Electron Microscope (FE-SEM) was explored to capture the images. All the images were captured with secondary electron detector. Energy-dispersive X-ray spectroscopy (EDX) was applied to know the elemental composition, while element content mapping allowed the determination of the distribution of elements of nickel oxide nanoflakes. Nickel oxide nanostructure samples were probed with diffused reflectance spectroscopy in the UV-vis-NIR region (190-1000 nm) to evaluate the wavelength-dependent modulation in optical behavior of as-grown samples. An Jasco-V770, equipped with a single monochromator design and 60 mm integrating sphere with PMT photodetector, was employed to perform the diffuse reflectance measurement at room temperature.

4.5 | Electrochemical measurements

The electrochemical deposition and characterization of all the samples were done using an Ametek Solartron Analytical (ModuLab XM) potentiostat. The electrochemical characterization was performed in three electrode system, where platinum wire, Ag/AgCl and microporous nickel/nickel oxide were used as counter, reference and working electrodes, respectively. In three electrode system, potential was measured between working electrode and reference electrode, and current was measured between working and counter electrode. Aqueous 3 M KOH was used as electrolyte for all electrochemical measurements. The areal capacitance (C_A), specific energy (E_A), and specific power (P_A) of nickel oxide nanoflakes were calculated from CV by using equations [48,55]

$$C_{A}\left(Fcm^{-2}\right) = \frac{\int_{-V}^{V} idV}{V\left(\frac{dV}{dt}\right)A}$$
 (6)

$$E_A \left(Whcm^{-2} \right) = \frac{1}{8 * 3600} C_{AV}^2$$
 (7)

$$P_{A}\left(Wcm^{-2}\right) = \frac{E_{A}}{V} \times \left(\frac{dV}{dt}\right) \times 3600$$
 (8)

where C_A is the areal capacitance (Fcm⁻²), V is the potential window (V), is $\frac{dV}{dt}$ the scan rate (V/s), and A is the area (cm²) of the electrode

ACKNOWLEDGMENT

The authors acknowledge, with pleasure, support from the National Science Foundation (NSF) with NSF-PREM grant #DMR-1827745.

CONFLICT OF INTEREST

The authors declare no conflict of interest.

DATA AVAILABILITY STATEMENT

The data that support the findings of this study are available from the corresponding author upon reasonable request.

SUPPORTING INFORMATION

The EDS data, elemental mapping, and diffuse reflectance data of Ni and NiO nanoflakes are presented in this supporting information, which is freely available at Wiley.com.

REFERENCES

1. S. Chu, A. Majumdar, Nature 2012, 488, 294.

- A. R. Rajalekshmi, M. L. Divya, S. Natarajan, V. Aravindan, Adv. Energy Sustain. Res. 2021, 2, 2000069.
- 3. D. G. Nocera, Chem. Soc. Rev. 2009, 38, 13.
- 4. Z. L. Wang, Adv. Mater. 2012, 24, 280.
- 5. P. Simon, Y. Gogotsi, Nat. Mater. 2008, 7, 845.
- Y. Shao, M. F. El-Kady, J. Sun, Y. Li, Q. Zhang, M. Zhu, H. Wang, B. Dunn, R. B. Kaner, *Chem. Rev.* 2018, 118, 9233.
- 7. J. Chen, P. S. Lee, Adv. Energy Mater. 2021, 11, 6.
- T. F. Yi, T. T. Wei, J. Mei, W. Zhang, Y. Zhu, Y. G. Liu, S. Luo, H. Liu, Y. Lu, Z. Guo, Adv. Sustain. Syst. 2020, 4, 1.
- 9. C. Liu, W. Zhou, J. Zhang, Z. Chen, S. Liu, Y. Zhang, J. Yang, L. Xu, W. Hu, Y. Chen, Y. Deng, Adv. Energy Mater. 2020, 10, 1.
- S. Zhumagali, F. H. Isikgor, P. Maity, J. Yin, E. Ugur, M. De Bastiani, A. S. Subbiah, A. J. Mirabelli, R. Azmi, G. T. Harrison, J. Troughton, E. Aydin, J. Liu, T. Allen, A. ur Rehman, D. Baran, O. F. Mohammed, S. De Wolf, *Adv. Energy Mater.* 2021, *11*, 1.
- 11. J. He, H. Lindström, A. Hagfeldt, S. E. Lindquist, *J. Phys. Chem. B* **1999**, *103*, 8940.
- 12. J. Wang, P. Yang, X. Wei, ACS Appl. Mater. Interfaces 2015, 7, 3816.
- Q. Wang, X. Huang, Z. L. Zhao, M. Wang, B. Xiang, J. Li, Z. Feng, H. Xu, M. Gu, J. Am. Chem. Soc. 2020, 142, 7425.
- V. S. Puli, C. Orozco, R. Picchini, C. V. Ramana, *Mater. Chem. Phys.* 2016, 184, 82.
- Y. Y. Sun, Y. Y. Wang, G. R. Li, S. Liu, X. P. Gao, ACS Appl. Mater. Interfaces 2019, 11, 14830.
- 16. K. C. Liu, M. A. Anderson, J. Electrochem. Soc. 1996, 143, 124.
- K.K. Bharathi, G. Markandeyulu, C.V. Ramana, J. Electrochem. Soc. 2011, 158, 71.
- Z. Luo, L. Liu, X. Yang, X. Luo, P. Bi, Z. Fu, A. Pang, W. Li, Y. Yi, ACS Appl. Mater. Interfaces 2020, 12, 39098.
- S. K. Meher, P. Justin, G. R. Rao, ACS Appl. Mater. Interfaces 2011, 3, 2063.
- S. I. Kim, J. S. Lee, H. J. Ahn, H. K. Song, J. H. Jang, ACS Appl. Mater. Interfaces 2013, 5, 1596.
- B. K. Singh, R. O. Dusane, S. Parida, *Mater. Sci. Eng. B* 2021, 273, 115436.
- V. S. Puli, R. Picchini, C. Orozco, C. V. Ramana, *Chem. Phys. Lett.* 2016, 649, 115.
- M. M. Sk, C. Y. Yue, K. Ghosh, R. K. Jena, J. Power Sources 2016, 308, 121.
- 24. T. Abzieher, S. Moghadamzadeh, F. Schackmar, H. Eggers, F. Sutterlüti, A. Farooq, D. Kojda, K. Habicht, R. Schmager, A. Mertens, R. Azmi, L. Klohr, J. A. Schwenzer, M. Hetterich, U. Lemmer, B. S. Richards, M. Powalla, U. W. Paetzold, *Adv. Energy Mater.* 2019, 9, 1.
- 25. M. S. Wu, G. W. Lin, R. S. Yang, J. Power Sources 2014, 272, 711.
- X. H. Xia, J. P. Tu, J. Zhang, X. L. Wang, W. K. Zhang, H. Huang, Sol. Energy Mater. Sol. Cells 2008, 92, 628.
- A. T. Gidey, D. W. Kuo, A. D. Fenta, C. T. Chen, C. T. Chen, ACS Appl. Energy Mater. 2021, 4, 6486.
- P. Kartikay, D. Sadhukhan, A. Yella, S. Mallick, Sol. Energy Mater. Sol. Cells 2021, 230, 111241.
- M. S. Wu, Y. A. Huang, C. H. Yang, J. J. Jow, Int. J. Hydrogen Energy 2007, 32, 4153.
- C. Li, M. Iqbal, J. Lin, X. Luo, B. Jiang, V. Malgras, K. C. W. Wu, J. Kim, Y. Yamauchi, *Acc. Chem. Res.* 2018, *51*, 1764.
- Z. Zhang, C. Feng, C. Liu, M. Zuo, L. Qin, X. Yan, Y. Xing, H. Li,
 R. Si, S. Zhou, J. Zeng, *Nat. Commun.* 2020, 11, 1.

- A. Biswal, P. K. Panda, A. N. Acharya, S. Mohapatra, N. Swain,
 B. C. Tripathy, Z. T. Jiang, M. Minakshi Sundaram, ACS Omega 2020, 5, 3405.
- T. Ozel, B. A. Zhang, R. Gao, R. W. Day, C. M. Lieber, D. G. Nocera, Nano Lett. 2017, 17, 4502.
- 34. S. Zhang, N. Pan, Adv. Energy Mater 2015, 5, 1.
- 35. J. Yan, S. Li, B. Lan, Y. Wu, P. S. Lee, *Adv. Funct. Mater.* **2020**, *30*, 1.
- A. Ferris, S. Garbarino, D. Guay, D. Pech, Adv. Mater. 2015, 27, 6625.
- M. Wang, A. C. Meng, J. Fu, A. C. Foucher, R. Serra-Maia, E. A. Stach, E. Detsi, J. H. Pikul, ACS Appl. Mater. Interfaces 2021, 13, 13097.
- B. K. Singh, A. Shaikh, S. Badrayyana, D. Mohapatra, R. O. Dusane, S. Parida, *RSC Adv.* 2016, 6, 100467.
- T. Fujita, P. Guan, K. Mckenna, X. Lang, A. Hirata, L. Zhang, T. Tokunaga, S. Arai, Y. Yamamoto, N. Tanaka, Y. Ishikawa, N. Asao, Y. Yamamoto, J. Erlebacher, M. Chen Nat. Mater. 2012, 11, 3391.
- Y. Zheng, J. Xu, Y. Zhu, T. Zhang, D. Yang, F. Qiu, *Inorg. Chem.* 2022, 61, 13.
- J.R. Deepak, V.K. B Raja, G.S. Kaliaraj, Results in Physics 2019, 14, 102437.
- 42. M. D. Abramoff, P. J. Magalhaes, S. J. Ram, *Biophotonics International*, **2004**, *11*, 36-42.
- C.V. Ramana, A. Ait-Salah, S. Utsunomiya, J.F. Morhange, A. Mauger, F. Gendron, C.M. Julien, J. Phys. Chem. C 2007, 111, 1049.
- 44. P. Kubelka, J. Opt. Soc. Am. 1948, 38, 448.
- 45. G. Gutierrez, E.M. Sundin, P.G. Nalam, V. Zade, R. Romero, A.N. Nair, S. Sreenivasan, D. Das, C. Li, C.V. Ramana, *J. Phys. Chem. C* **2021**, *125*, 20468.
- C.V. Ramana, G. Carbajal-Franco, R.S. Vemuri, I.B. Troitskaia,
 S.A. Gromilov, V.V. Atuchin, *Mater. Sci. Eng. B* 2021, 174, 279.
- 47. V.H. Mudavakkat, V.V. Atuchin, V.N. Kruchinin, A. Kayani, C.V. Ramana, *Opt. Mater.* **2012**, *34*, 893.
- 48. U. K. Chime, A. C. Nkele, S. Ezugwu, A. C. Nwanya, N. M. Shinde, M. Kebede, P. M. Ejikeme, M. Maaza, F. I. Ezema, *Curr. Opin. Electrochem.* **2020**, *21*, 175.
- 49. B. K. Singh, A. Shaikh, R. O. Dusane, S. Parida, *J. Energy Storage* **2020**, *31*, 1.
- 50. B. K. Singh, A. Shaikh, R. O. Dusane, S. Parida, *Nano-Structures & Nano-Objects* **2019**, *17*, 239.
- Y. Xu, A. S. Menon, P. P. R. M. L. Harks, D. C. Hermes, L. A. Haverkate, S. Unnikrishnan, F. M. Mulder, *Energy Storage Mater.* 2018, 12, 69.
- 52. D. Tench, L. F. Warren, J. Electrochem. Soc. 1983, 130, 869.
- H. Ji, X. Zhao, Z. Qiao, J. Jung, Y. Zhu, Y. Lu, L. L. Zhang, A. H. MacDonald, R. S. Ruoff, *Nat. Commun.* 2014, 5, 3317.
- A. K. Singh, D. Sarkar, G. G. Khan, K. Mandal, J. Mater. Chem. A 2013, I, 12759.
- X. Sun, G. Wang, J. Y. Hwang, J. Lian, J. Mater. Chem. 2011, 21, 16581.
- I. E. Rauda, V. Augustyn, B. Dunn, S. H. Tolbert, *Acc. Chem. Res.* 2013, 46, 1113.
- G. Wang, H. Wang, X. Lu, Y. Ling, M. Yu, T. Zhai, Y. Tong, Y. Li, Adv. Mater. 2014, 26, 2676.
- L. Su, L. Gao, Q. Du, L. Hou, Z. Ma, X. Qin, G. Shao, J. Alloys Compd. 2018, 749, 900.



- 59. J. Zhao, X. Shu, Y. Wang, C. Yu, J. Zhang, J. Cui, Y. Qin, H. Zheng, J. Liu, Y. Zhang, Y. Wu, Surf. Coatings Technol. 2016, 299, 15.
- 60. Y. Chen, Y. Wang, P. Sun, P. Yang, L. Du, W. Mai, *J. Mater. Chem. A* **2015**, *3*, 20614.
- 61. J. Liu, J. Jiang, M. Bosman, H. J. Fan, J. Mater. Chem. 2012, 22,
- B. S. Soram, J. Dai, T. Kshetri, N. H. Kim, J. H. Lee, *Chem. Eng. J.* 2020, 391, 123540.
- 63. J. Lu, H. Ran, J. Li, J. Wan, C. Wang, P. Ji, X. Wang, G. Liu, C. Hu, *Electrochim. Acta* **2020**, *331*, 135426.
- H. Zhang, J. Wei, Y. Yan, Q. Guo, L. Xie, Z. Yang, J. He, W. Qi, Z. Cao, X. Zhao, P. Pan, H. Li, K. Zhang, J. Zhao, X. Li, P. Zhang, K. W. Shah, *J. Power Sources* 2020, 450, 227616.

SUPPORTING INFORMATION

Additional supporting information can be found online in the Supporting Information section at the end of this article.

How to cite this article: B. Kr. Singh, D. Das, N. Attarzadeh, S. N. Chintalapalle, C. V. Ramana, *Nano Select.* **2023**, *4*, 145.

https://doi.org/10.1002/nano.202200180